metals

MDPI

Article

TiAl Alloy Fabricated Using Election Beam Selective Melting: Process, Microstructure, and Tensile Performance

Yu Zhang [1,2], Yan Li [2], Meihui Song [2,*], Yanchun Li [2], Shulin Gong [2] and Bin Zhang [1,*]

[1] Postdoctoral Mobile Station, Harbin Engineering University, Harbin 150000, China
[2] Institute of Advanced Technology, Heilongjiang Academy of Sciences, Harbin 150000, China
* Correspondence: zhangyunjust@163.com (M.S.); zhangbin6413@hotmail.com (B.Z.)

Abstract: TiAl alloy is one of the most attractive candidates for a new generation of high-temperature structural materials and has broad application prospects in the aerospace field. As a typical intermetallic material, TiAl is inevitably difficult to process using conventional methods. Election beam selective melting (EBSM) is an effective method of addictive manufacturing to prepare TiAl alloy with a complex structure. However, the microstructure of TiAl alloy formed using EBSM often contains defects such as pores, which seriously reduces the mechanical properties of the material. In this work, the effects of EBSM and post-processing procedures on the microstructure and mechanical properties of Ti-48Al-2Cr-2Nb alloy were studied. The results show that the microstructure of Ti-48Al-2Cr-2Nb alloy formed using the EBSM process was dense and composed of equiaxed γ-phase and double-phase regions. A large number of dislocations that formed due to thermal stress were clearly observed inside the Ti-48Al-2Cr-2Nb alloy. When the EBSM process parameters were 13.5 mA, 4.0 m/s, and 40.50 J/mm^3, as the current intensity increased, the Al content decreased, the content of α_2 phase increased, and the microstructure of the material was coarse. The results of the tensile test fracture morphology indicate that the Ti-48Al-2Cr-2Nb alloy exhibited brittle fracture during tensile deformation, lacking the typical yield deformation of metal materials. As the energy density of the EBSM process increased, the mechanical properties of the Ti-48Al-2Cr-2Nb alloy first increased and then decreased. The samples prepared with an energy density of 34.50~40.50 J/mm^3 had excellent mechanical properties, of which the maximum tensile strength and maximum elongation reached 643 MPa and 2.09%, respectively. The phase composition of the Ti-48Al-2Cr-2Nb alloy after hot isostatic pressing (HIP) treatment remained unchanged from the EBSM samples, but there was a slight difference in content. There was an increase in the amount of γ phase and a decrease in B2 phase, accompanied by the generation of a massive γ phase after HIP treatment. Moreover, the number of dislocations inside the material increased. The Ti-48Al-2Cr-2Nb alloy after HIP treatment exhibited obvious plastic deformation characteristics, with a tensile strength of 679 MPa and elongation of 2.5%. A heat treatment of 900 °C/5 h was performed on the Ti-48Al-2Cr-2Nb alloy after HIP. The dislocation density of the Ti-48Al-2Cr-2Nb alloy decreased, and the B2 phase transformed from massive to lamellar.

Keywords: TiAl alloy; electron beam selective melting (EBSM); post-processing; microstructure; tensile performance

Citation: Zhang, Y.; Li, Y.; Song, M.; Li, Y.; Gong, S.; Zhang, B. TiAl Alloy Fabricated Using Election Beam Selective Melting: Process, Microstructure, and Tensile Performance. *Metals* **2024**, *14*, 482. https://doi.org/10.3390/met14040482

Academic Editor: Irene Buj Corral

Received: 11 March 2024
Revised: 15 April 2024
Accepted: 18 April 2024
Published: 20 April 2024

1. Introduction

TiAl alloy has many advantages, such as a low density, high specific modulus, good mechanical properties at high temperature, creep resistance, oxidation resistance at 900 °C, and flame-retardant properties [1–4]. It is one of the most attractive candidates for a new generation of high-temperature structural materials for aero engines and rocket propulsion systems. At the same time, it is also one of the suitable materials for the development of supersonic aircraft [5]. TiAl alloy has been successfully used in aviation and automotive engines. The traditional casting method leads to a coarse structure of TiAl alloy, which

can easily form porosity and component segregation inside, resulting in poor mechanical properties. In addition, the low-room-temperature plasticity of TiAl alloy makes some traditional processing methods, such as rolling, forging, and turning, very difficult [6–8]. The poor ductility is linked to issues inherent in the material, i.e., from the lack of slip systems in the long range ordered phases present at room temperature. The large lamellar grain sizes and elemental segregation are also challenges for the casting TiAl alloy. Therefore, reducing processing steps would be of industrial interest. Compared to traditional manufacturing technology, the biggest advantage of additive manufacturing (AM) technology is that it can realize the near-net formation of complex parts, which has no requirement for the geometric complexity of parts and the subsequent machining process [9–11]. Deformation and cracking in the additive manufacturing process can be effectively prevented.

The main AM methods for TiAl alloys include laser metal deposition (LMD), selective laser melting (SLM), and electron beam melting (EBM) [12–14]. Both LMD technology and SLM technology use laser beams to melt metal powders and belong to the field of laser additive manufacturing, while EBM technology uses electron beams as energy sources [15–17]. However, the research results show that it is difficult to form TiAl alloy using laser additive manufacturing, and the formed parts are prone to cracks. Compared to laser additive manufacturing technology, TiAl alloy prepared using EBM technology has low impurity (oxygen and nitrogen) contents, no cracks, low porosity, and a high density of more than 98% [18]. However, during the EBM forming process, when the energy is high, Al is prone to volatilization, causing a change in the alloy composition and thus affecting the performance of the alloy [19,20].

In this article, the electron beam selective melting (EBSM) process was used to form TiAl alloy, after which post-processing was carried out. The effects of EBSM and post-processing on the microstructure and tensile properties of TiAl alloy were investigated.

2. Materials and Methods

2.1. Raw Material

The authors used the plasma rotate electrode process (PREP) for the AM of Ti-48Al-2Cr-2Nb (at. %) spherical powder. The composition of the powder is shown in Table 1. It can be seen in the table that the content of the element in the powder met the requirements of the brand, and there was no loss of alloy elements. The stability of the element content is a prerequisite for the subsequent EBSM process, ensuring the excellent performance of the material. The particle size distribution and morphology of the powder are shown in Figure 1. The size range of the powder was 37~123 μm, as shown in Figure 1a. In Figure 1b, we can see that the particles of the Ti-48Al-2Cr-2Nb alloy were spherical, with few irregular shapes. At the same time, there were no satellite-shaped particles or other defects.

Table 1. Alloy element contents of the powder.

Element	Mass Fraction (wt. %)	Composition in at. %
Ti	59.02	47.84
Al	33.47	48.16
Cr	2.61	1.95
Nb	4.89	2.04
Total	100.00	100.00

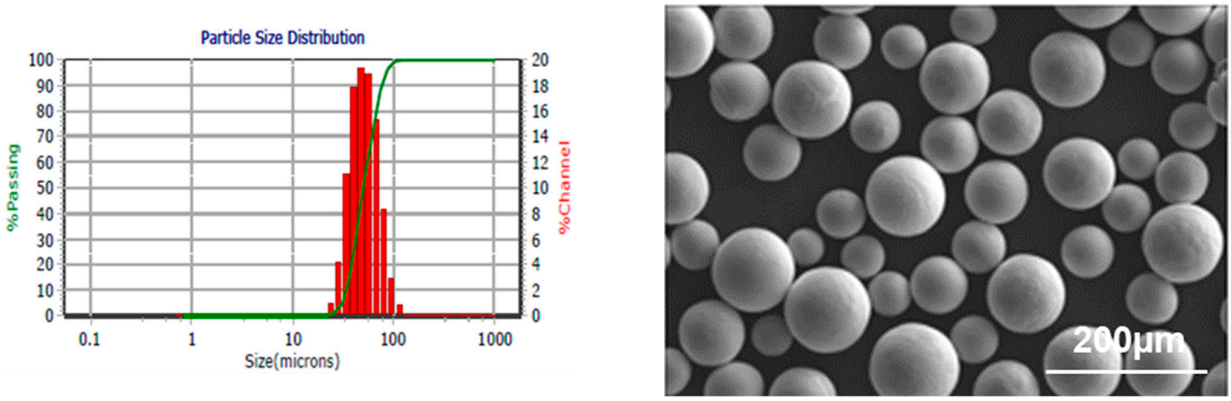

(**a**) (**b**)

Figure 1. Images of Ti-48Al-2Cr-2Nb powder: (**a**) particle size distribution; (**b**) SEM photograph.

2.2. EBSM and Post-Processing

The specimens were produced with the EBSM system in a vacuum of 10^{-3} Pa, using He as shielding gas. The electron beam voltage was 60 kV. The influence of the EBSM process parameters on the dimensional accuracy, formation of defects, microstructure, and mechanical properties of the alloys was evaluated as a function of different input energy densities (E_v), as given by the following [21]:

$$E_v = UI/(vdh) \quad (1)$$

where U is the accelerating voltage, I is the beam current, v is the scanning speed, d is the scanning gap, and h is the layer thickness. The main process parameters of EBSM are shown in Table 2. For the melting process, the samples were scanned using a snaking route, with the scan line rotated 90 ° between each layer (Figure 2).

Table 2. The main process parameters of EBSM.

Number	Beam Current (mA)	Scanning Speed (m/s)	Scanning Gap (mm)	Layer Thickness (mm)	Energy Density (J/mm^3)
1	12.5	4.5	0.1	0.05	33.33
2	11.5	4	0.1	0.05	34.50
3	14.5	4.5	0.1	0.05	38.67
4	13.5	4	0.1	0.05	40.50

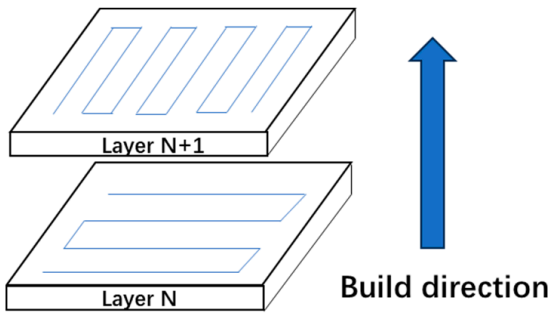

Figure 2. Schematic illustration of the scanning method.

In order to reduce the internal stress of the formed specimens and improve the strength and elongation of the material, the specimens were subjected to post-processing: heat treatment (HT; 900 °C/5 h), hot isostatic pressing (HIP; 1260 °C, 150 MPa/4 h), and HIP + HT.

2.3. Microstructural Characterization and Mechanical Testing

The particle size distribution and morphology of the Ti-48Al-2Cr-2Nb powder was characterized using the Microtrac S3500 laser particle analyzer and the FEI-Sirion scanning electron microscope (SEM), respectively. The microstructure of the specimens was observed with the Carl Zeiss-Axio Vert. A1 metallographic microscope, the S4700 and FEI-Sirion scanning electron microscope (SEM), and the JEM-2100 transmission electron microscope (TEM). The phase composition of the samples was characterized using the X Pert3 Powder X-ray diffractometer (Cu K_α, scanning rate of 3°/min, scanning range of 30–100°).

The tensile test samples were taken and processed from a rectangular-shaped sample with a length of 80 mm, a width of 18 mm, and a height of 40 mm, as shown in Figure 3a. The tensile test was carried out at room temperature with a constant speed of 4 mm/min using a WDW-E tensile testing machine. The strain was measured with an extensometer. The gauge size of each sample was 20 mm, and the diameter was 5 mm, as shown in Figure 3b. The tensile test samples are schematically shown in Figure 3c.

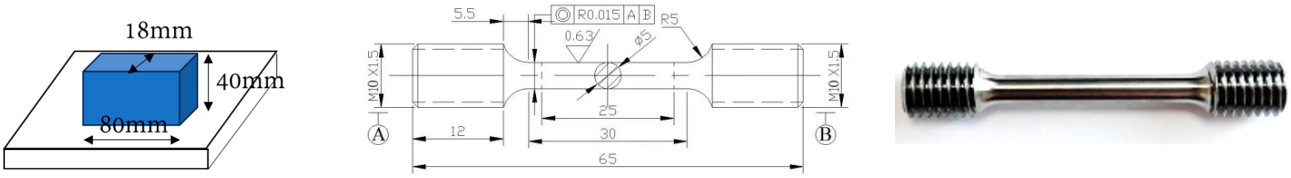

(**a**) (**b**) (**c**)

Figure 3. Tensile test samples: (**a**) sampling; (**b**) dimensions (unit: mm); (**c**) image.

3. Results and Discussion

3.1. Effect of EBSM Process on Microstructure of Ti-48Al-2Cr-2Nb Alloy

3.1.1. Phase Composition

Figure 4 shows the XRD diffraction patterns of the Ti-48Al-2Cr-2Nb alloy formed using different EBSM process parameters. It can be seen in the diagram that the phase structure of the Ti-48Al-2Cr-2Nb alloy was composed of γ phase and α_2 phase. When the scanning rate was 4.0 m/s, the current beam intensity of the electron beam was higher, and the γ (111) diffraction peak was stronger. However, when the scanning rate was 4.5 m/s, the results were the opposite. In addition, when the process parameters were 13.5 mA, 4.0 m/s, and 40.50 J/mm^3, it can clearly be seen that α_2 phase diffraction peaks appeared in the spectrum. The above results show that the α_2 phase content increased with the increase in the beam current intensity.

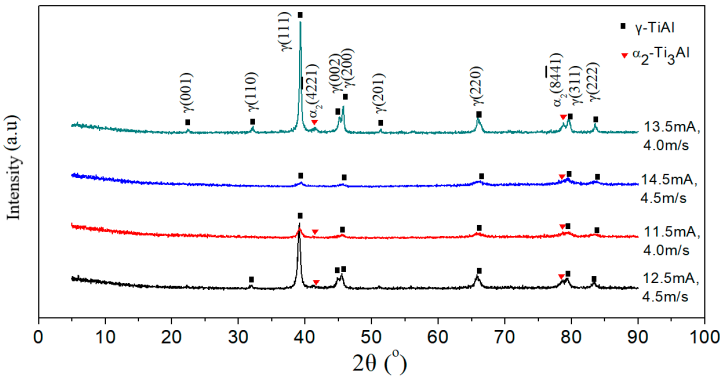

Figure 4. The effect of the EBSM process parameters on the XRD diffraction pattern of Ti-48Al-2Cr-2Nb alloy.

3.1.2. Microstructure of Ti-48Al-2Cr-2Nb Alloy Formed Using EBSM Process

Figure 5 shows the effect of the EBSM process on the pores of the Ti-48Al-2Cr-2Nb alloy. It can be seen in Figure 5a that there were many pores in the TiAl alloy formed with the parameters of 12.5 mA, 4.5 m/s, and 33.33 J/mm^3. As the energy density increased, the number of pores gradually decreased. No pores were observed in the Ti-48Al-2Cr-2Nb alloy formed with the process parameters of 14.5 mA, 4.5 m/s, and 38.67 J/mm^3 (Figure 5c). It can be seen that the internal pores of the material gradually decreased and eventually disappeared when the energy density increased to 40.50 J/mm^3. The relative densities of the samples formed using EBSM with different parameters are shown in Table 3. As the energy density increased, the metal particles melted more extensively and infiltrated each other, which was beneficial for improving the uniformity and compactness of the material [22].

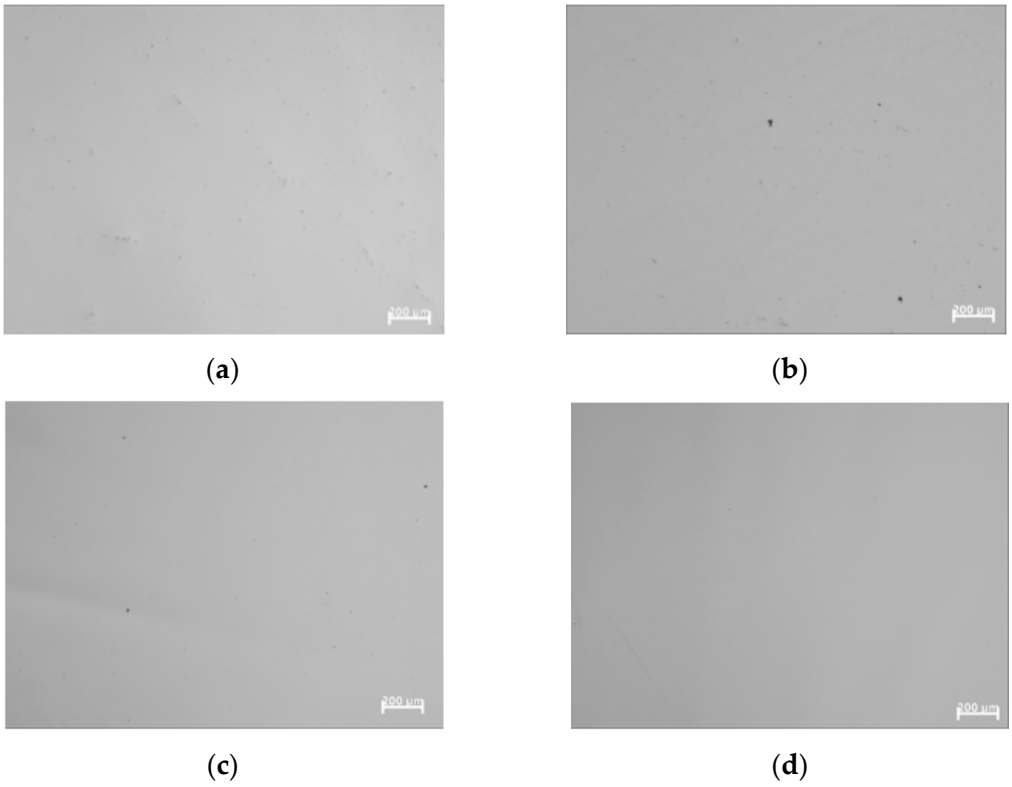

Figure 5. The effect of the EBSM process on the pores in the Ti-48Al-2Cr-2Nb alloy: (**a**) 12.5 mA, 4.5 m/s, and 33.33 J/mm^3; (**b**) 11.5 mA, 4.0 m/s, and 34.5 J/mm^3; (**c**) 14.5 mA, 4.5 m/s, and 38.67 J/mm^3; (**d**) 13.5 mA, 4.0 m/s, and 40.50 J/mm^3.

Table 3. The relative densities of the samples formed using EBSM with different parameters.

Sample Number	Energy Density (J/mm^3)	Relative Density (%)	Porosity (%)
1	33.33	97.3	2.7
2	34.50	98.1	1.9
3	38.67	99.3	0.7
4	40.50	99.4	0.6

Figure 6 shows the effect of the EBSM process on the metallographic structure of the Ti-48Al-2Cr-2Nb alloy. It can be seen in the figure that the Ti-48Al-2Cr-2Nb alloy prepared using EBSM was mainly composed of equiaxed γ phases and lamellar-structured α_2/γ double phases. The phase composition was mainly related to the thermal conductivity of the layer-by-layer stacking process of EBSM [23]. The nth layer of the material underwent cyclic heat treatment at a high temperature and finally stabilized in the double-phase

region of α_2/γ slightly above the eutectoid transition temperature (1150 °C) [24]. However, this microstructure exhibited non-uniformity, which was due to the dramatic change in the temperature field around the molten pools during the EBSM forming process [25]. The solidification path of the Ti-48Al-2Cr-2Nb alloy was mainly determined by its kinetic factors. During the equilibrium solidification of alloys containing 48 at. % Al, the α phase in the liquid phase L nucleates and grows, and the γ-phase precipitates from the α phase [26]. However, during the EBSM process, Al evaporates from the top of the melt [27]. This difference in chemical composition cannot be compensated for via diffusion during rapid solidification. L → L + β occurs in the upper region of the melt pool, while in the other regions, L → L + α. As the temperature continues to decrease, the β phase transforms into the α phase, but some of the β phase may be retained under rapid cooling conditions. Due to the small size of EBSM molten pools with rapid cooling characteristics, the phase transition process during solidification often deviates from thermodynamic equilibrium [28]. The phase transition path is $L \rightarrow L + \beta \rightarrow \beta \rightarrow \beta + \alpha \rightarrow \alpha \rightarrow \alpha_2 + \beta$ [29].

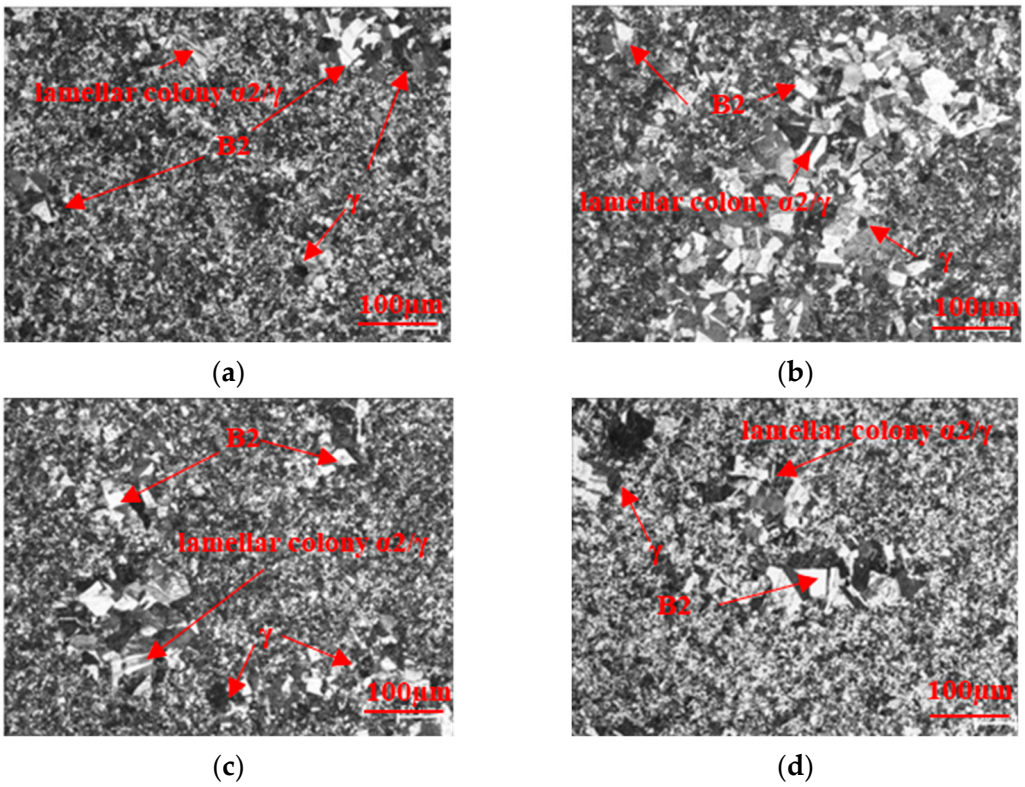

Figure 6. The effect of the EBSM process on the metallographic structure of the Ti-48Al-2Cr-2Nb alloy: (**a**) 12.5 mA, 4.5 m/s, and 33.33 J/mm^3; (**b**) 11.5 mA, 4.0 m/s, and 34.5 J/mm^3; (**c**) 14.5 mA, 4.5 m/s, and 38.67 J/mm^3; (**d**) 13.5 mA, 4.0 m/s, and 40.50 J/mm^3.

During the process of $\alpha \rightarrow \alpha_2 + \gamma$, lamellar α phases and γ phases precipitated at the same time. The grain sizes of the samples fabricated using EBSM are listed in Table 4. In the table, we can see that when the scanning speed was the same, the electron beam current intensity was higher, the grain was coarser, and there were more α_2/γ double phases. In addition, the grain size is related to the cooling rate. Generally, a high cooling rate and short solidification process duration results in finer grains [30]. With a cooling rate of 10^3–10^5 K/s, a predominance of fine grains was obtained after the fast solidification process using EBSM [31,32].

Table 4. The grain sizes of the samples fabricated using EBSM.

Sample Number	Energy Density (J/mm^3)	Grain Size (μm)
1	33.33	4.7
2	34.50	5.6
3	38.67	6.9
4	40.50	7.3

To further investigate the phase composition in the Ti-48Al-2Cr-2Nb alloy, TEM observation was carried out, and the results are shown in Figure 7. Some fine lamellar structures consisting of α_2/γ double phases can be observed in Figure 7a. Moreover, equiaxed γ phases were at the edge of the lamellar grains, and some B2 phases formed by the ordering of the β phases [33]. In addition, the α_2 phase was mainly distributed at the junction of the grain boundaries, which were not discontinuous (Figure 7b). A large number of dislocations formed due to thermal stress were also observed inside the 48Al-2Cr-2Nb alloy (Figure 7c).

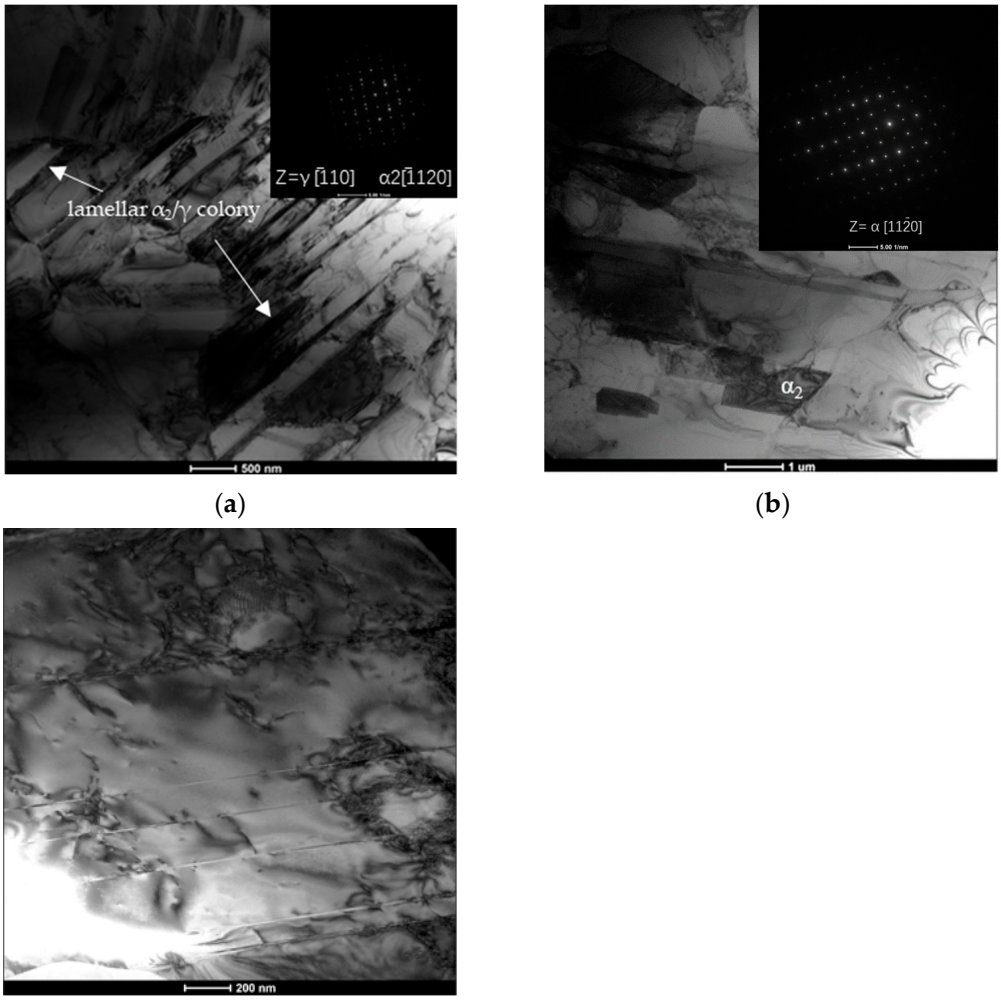

Figure 7. TEM microstructure of Ti-48Al-2Cr-2Nb alloy with process parameters of 13.5 mA, 4.0 m/s, and 40.50 J/mm^3: (**a**) lamellar structure; (**b**) distribution of α_2 phases; (**c**) dislocations.

TEM and EDS were employed to study the dark field images of the equiaxed γ phases, as shown in Figure 8. As can be seen in the figure, there were areas with lower brightness between the bright and wide lamellar γ phases (Figure 8a). EDS analysis revealed that

the elemental composition of the region was mainly Ti and Al (Figure 8b), with an atomic ratio close to 2:1. This indicates that the lamellar phases between the equiaxed γ phases were B2 phases. The formation of B2 phases was due to the high cooling rate and short solidification process duration during the preparation of the Ti-48Al-2Cr-2Nb alloy [34]. Because the cooling rate was so high, the α_2 phases could not be completely transformed into γ phases during the fast solidification process, and B2 phases were generated.

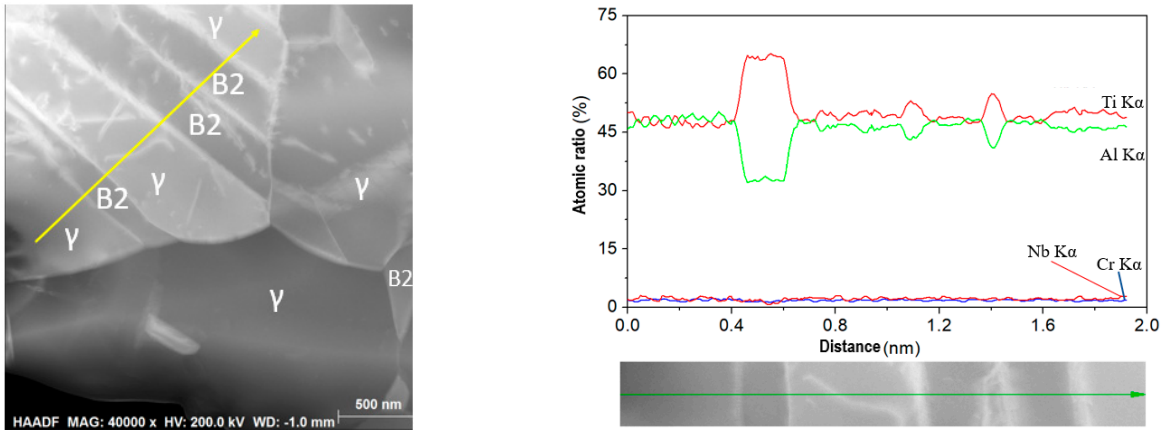

(**a**) (**b**)

Figure 8. Equiaxed γ phases in Ti−48Al−2Cr−2Nb alloy with process parameters of 13.5 mA, 4.0 m/s, and 40.50 J/mm^3: (**a**) dark field images; (**b**) EDS analysis of the lineation zone.

3.1.3. Element Distribution of Ti-48Al-2Cr-2Nb Alloy Formed Using EBSM Process

Figure 9 shows the element distribution of the Ti-48Al-2Cr-2Nb alloy. As shown in the figure, alloy elements such as Al, Nb, and Cr were evenly distributed inside the material without segregation. Table 5 shows the effect of the EBSM process on the element contents of the Ti-48Al-2Cr-2Nb alloy. It can be seen in Table 5 that when the scanning rate was 4.0 m/s, the beam current intensity increased and the Al content decreased, indicating that Al was lost during the forming process, which is mainly related to the energy density. When the scanning rate was the same, the beam current intensity increased, the energy density increased, and the surface temperature of the liquid metal increased, making the Al more volatile. However, when the scanning rate was 4.5 m/s, the element content in the alloy did not change significantly. This is because in the fast solidification process, the effect of the formation process on the surface temperature of the material is relatively small, so the volatilization rate of the elements is basically the same [35]. In addition, by comparing the element contents of the powder and the Ti-48Al-2Cr-2Nb alloy formed using the EBSM process in Table 5, it can be seen that Al exhibited volatilization with different forming processes, but the element contents of the final formed parts prepared in this study meet the Chinese national standard for the composition of TiAl alloy (GB/T 3620.1-2016) [36].

Table 5. Effect of EBSM process on element content of Ti-48Al-2Cr-2Nb alloy (wt.%).

Element	Powder	12.5 mA, 4.5 m/s, 33.33J/mm^3	11.5 mA, 4.0 m/s, 34.50 J/mm^3	14.5 mA, 4.5 m/s, 38.67 J/mm^3	13.5 mA, 4.0 m/s, 40.50 J/mm^3
Al	34.26	31.31	31.39	31.49	29.89
Ti	57.59	60.51	60.70	60.71	62.09
Cr	2.62	2.37	2.35	2.34	2.32
Nb	5.53	5.81	5.56	5.46	5.71
Total	100.00	100.00	100.00	100.00	100.00

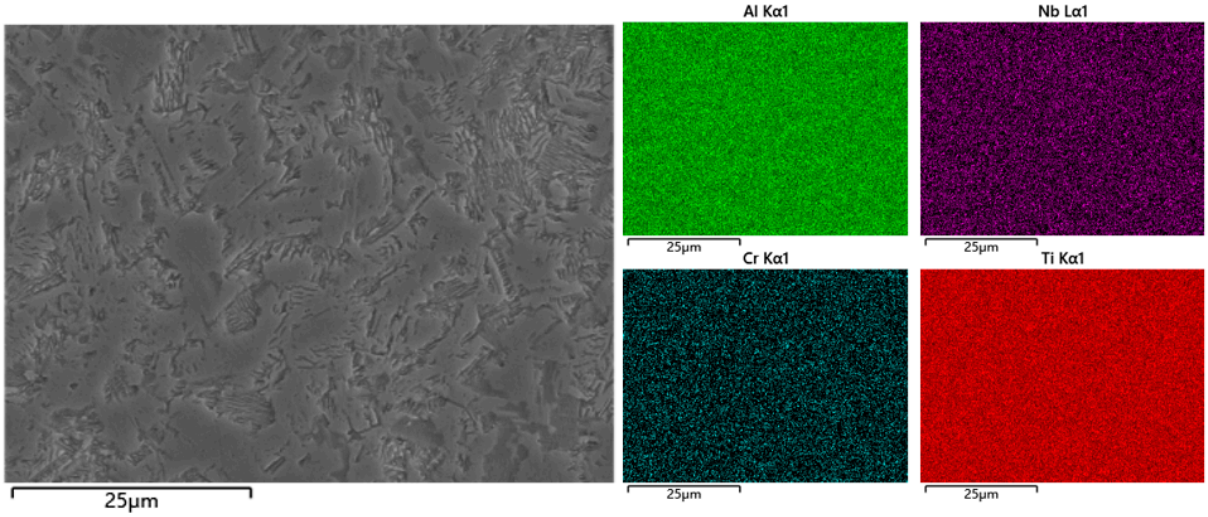

(**a**)

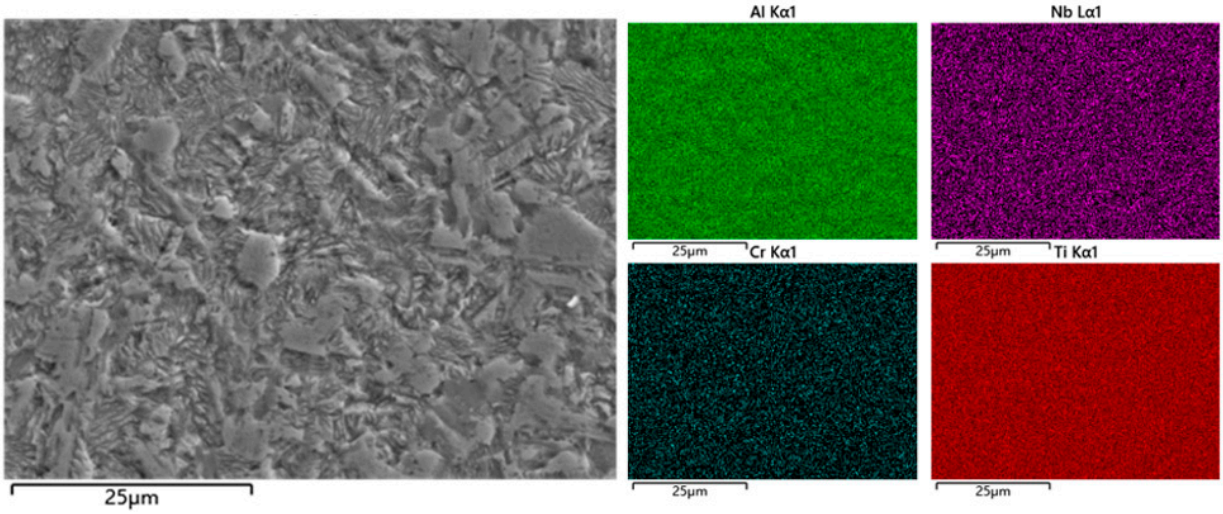

(**b**)

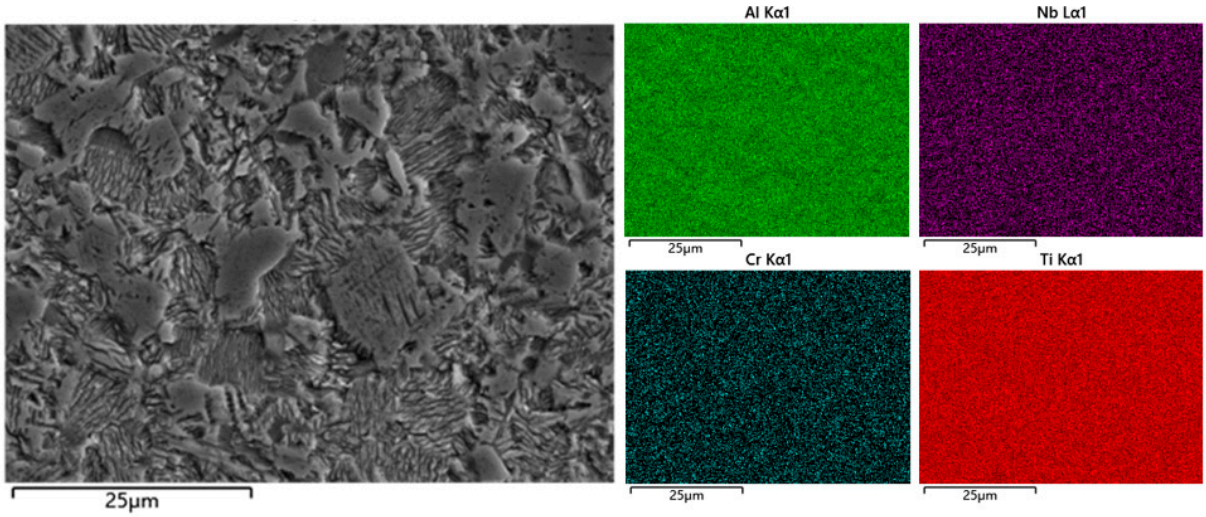

(**c**)

Figure 9. *Cont*.

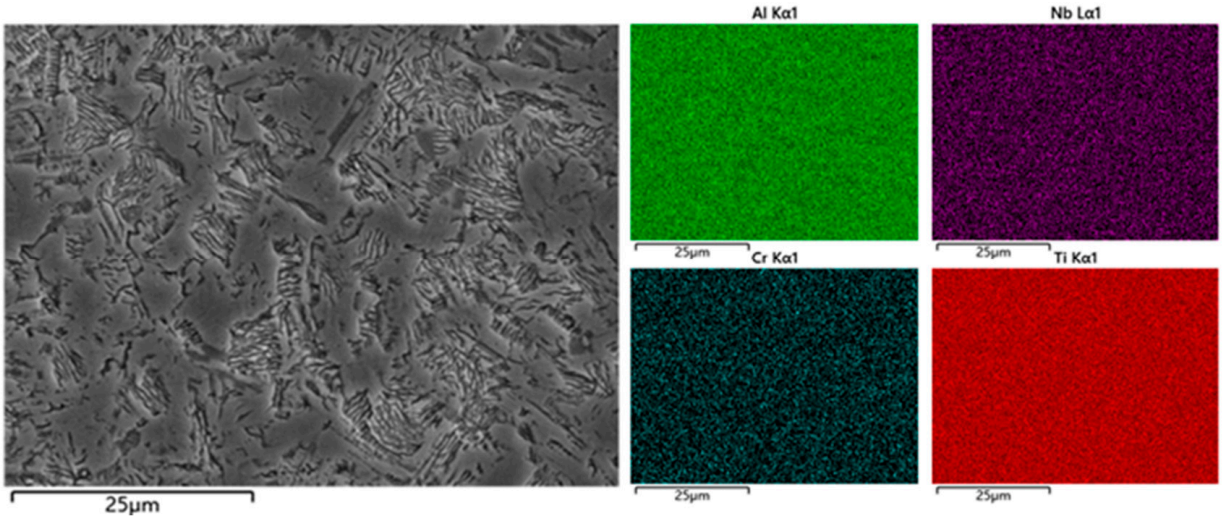

(**d**)

Figure 9. Effect of EBSM process on element distribution of Ti-48Al-2Cr-2Nb alloy: (**a**) 12.5 mA, 4.5 m/s, and 33.33 J/mm^3; (**b**) 11.5 mA, 4.0 m/s, and 34.5 J/mm^3; (**c**) 14.5 mA, 4.5 m/s, and 38.67 J/mm^3; (**d**) 13.5 mA, 4.0 m/s, and 40.50 J/mm^3.

3.2. Effect of EBSM Process on Mechanical Properties of Ti-48Al-2Cr-2Nb Alloy

Figure 10 shows the room-temperature tensile properties of the Ti-48Al-2Cr-2Nb alloy formed using the EBSM process with different input energy densities. As shown in the figure, all the samples exhibited brittle fracture during tensile deformation, lacking the typical yield deformation of metal materials. The tensile strengths of the samples are listed in Table 6, where it can be seen that as the energy density increased, the tensile properties of the Ti-48Al-2Cr-2Nb alloy first increased and then decreased. The maximums of the tensile properties and elongation were 643 MPa and 2.09%, respectively. As shown in Table 3, as the energy density increased, the number of pores in the Ti-48Al-2Cr-2Nb alloy decreased, thus improving its tensile properties. However, when the energy density was too high, over-firing occurred and a coarse microstructure was generated in the alloy, leading to a decrease in its tensile properties [37]. At the same time, the contents of α_2 and B2 phases were higher than those in other samples. In this study, the tensile strengths and elongation rates of the samples prepared with an energy density of 34.50–40.50 J/mm^3 were over 620 MPa and 1.9%, respectively.

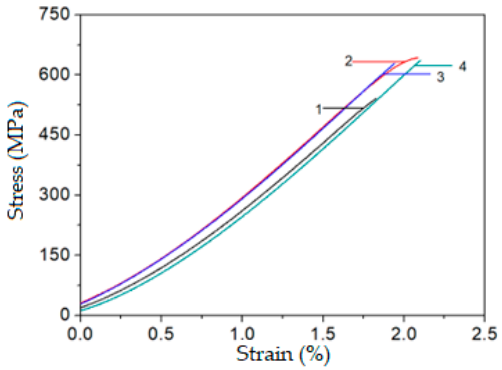

Figure 10. Comparison of room-temperature tensile properties of Ti-48Al-2Cr-2Nb alloy formed using EBSM process with different input energy densities: (1) 12.5 mA, 4.5 m/s, and 33.33 J/mm^3; (2) 11.5 mA, 4.0 m/s, and 34.5 J/mm^3; (3) 14.5 mA, 4.5 m/s, and 38.67 J/mm^3; (4) 13.5 mA, 4.0 m/s, and 40.50 J/mm^3.

Table 6. Tensile properties of Ti-48Al-2Cr-2Nb alloy formed with different energy densities.

Number	Process Parameters	Energy Density (J)	Tensile Strength (MPa)	Elongation after Fracture (%)
1	12.5 mA, 4.5 m/s	33.33	541	1.82
2	11.5 mA, 4.0 m/s	34.50	643	2.09
3	14.5 mA, 4.5 m/s	38.67	628	1.94
4	13.5 mA, 4.0 m/s	40.50	633	2.01

Figure 11 reflects the effect of the EBSM process on the tensile fracture of the Ti-48Al-2Cr-2Nb alloy. It can clearly be seen that the fracture surface of the Ti-48Al-2Cr-2Nb alloy exhibited typical brittle fracture characteristics without ductile dimples or tearing edges, which is consistent with the results of the tensile curves (as shown in Figure 11). The fracture failure of the Ti-48Al-2Cr-2Nb alloy sample exhibited typical brittle characteristics. Four main fracture modes were present: intergranular, cleavage, trans-lamellar, and interlamellar. The fracture morphologies of the samples were composed of a large number of small fracture surfaces, including multiple fracture modes. The four fracture modes mentioned above were reflected in all samples.

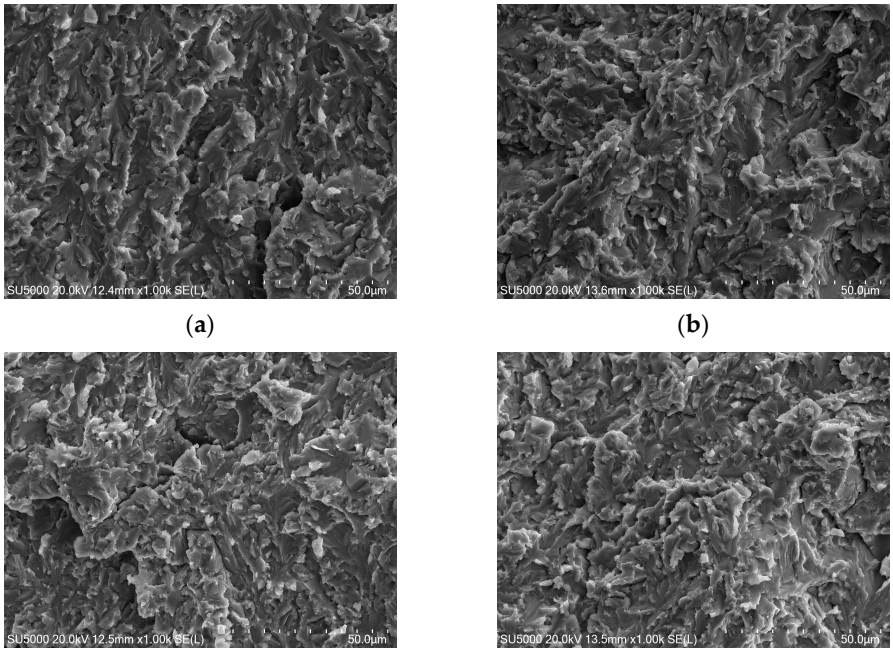

Figure 11. Tensile fracture morphology of Ti-48Al-2Cr-2Nb alloy: (**a**) 12.5 mA, 4.5 m/s, and 33.33 J/mm^3; (**b**) 11.5 mA, 4.0 m/s, and 34.5 J/mm^3; (**c**) 14.5 mA, 4.5 m/s, and 38.67 J/mm^3; (**d**) 13.5 mA, 4.0 m/s, and 40.50 J/mm^3.

3.3. Anisotropy Analysis of Microstructure and Mechanical Properties of Ti-48Al-2Cr-2Nb Alloy Formed Using EBSM

During the EBSM process, an electron beam heats the powder until it melts and bonds together; then, it cools and solidifies to form a solid block-like material sample. The internal temperature of the sample is transmitted to the bottom substrate through thermal diffusion, resulting in a top-down heat flow and temperature gradient in the direction of the material preparation, which affects the microstructure and properties of the material [38]. In previous studies, the longitudinal microstructure and properties of the materials were discussed and analyzed. In this section, the differences in the microstructures and mechanical properties of the EBSM-formed Ti-48Al-2Cr-2Nb alloy in both the transverse and longitudinal directions are analyzed and discussed.

3.3.1. Anisotropy of Microstructure of Ti-48Al-2Cr-2Nb Alloy Formed Using EBSM

Figure 12 shows the metallographic structure of the EBSM-formed TiAl alloy in different directions. As shown in the figure, there was not much of a difference between the transverse metallographic structure and the longitudinal metallographic structure (Figure 12a–d). Clear dual-phase structures can be observed at both low and high magnification.

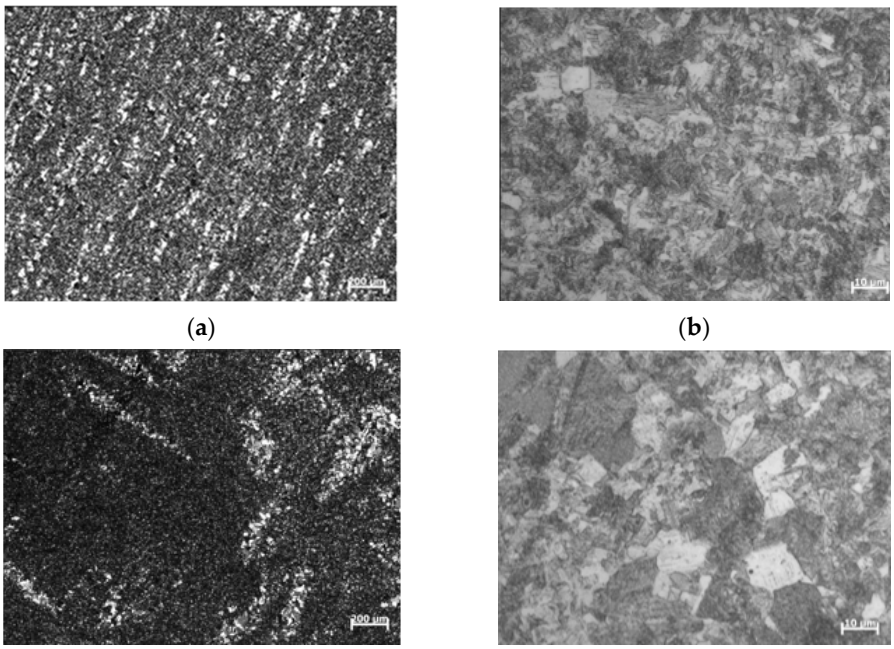

Figure 12. Metallographic structure of Ti-48Al-2Cr-2Nb alloy formed using EBSM in different directions: (**a**) transverse, low magnification; (**b**) transverse, high magnification; (**c**) longitudinal, low magnification; (**d**) longitudinal, high magnification.

EBSD was used to analyze the grain size of TiAl alloy, and the results are shown in Figure 13. Comparing Figure 13a,b, it can be seen that the results are the same as those of the metallographic structure analysis, and the transverse and longitudinal grain sizes are not much different.

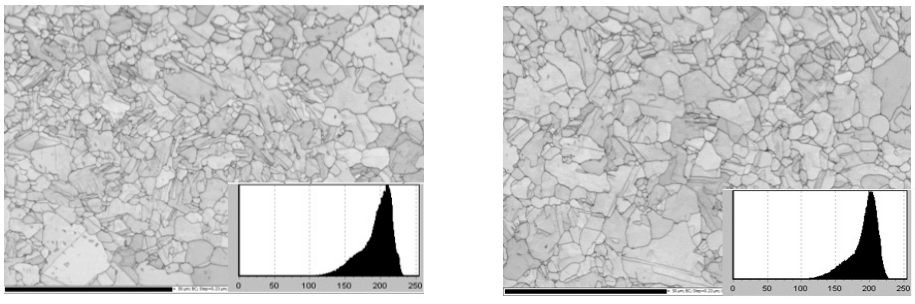

Figure 13. Analysis of grain sizes in different directions of Ti-48Al-2Cr-2Nb alloy: (**a**) transverse direction; (**b**) longitudinal direction.

3.3.2. Anisotropy of Mechanical Properties of Ti-48Al-2Cr-2Nb Alloy Formed Using EBSM

Figure 14 shows the mechanical properties of the TiAl alloy in different directions after EBSM. It can be seen in the figure that the transverse and longitudinal mechanical properties of the TiAl alloy prepared in this study were not much different. The transverse and longitudinal tensile strengths of the alloy were 625 MPa and 637 MPa, respectively. The

transverse and longitudinal elongations of the alloy were 2.3% and 2.1%, respectively. It can be seen in Figures 12 and 13 that the microstructure of the material in different directions was not much different, resulting in its anisotropy being not obvious, so the mechanical properties of the material in different directions were not very diverse.

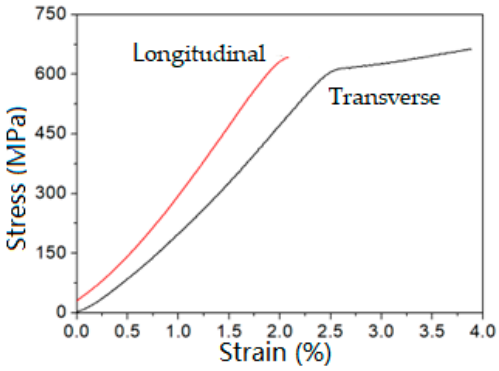

Figure 14. Tensile properties of Ti-48Al-2Cr-2Nb alloy formed using EBSM processes in different directions.

3.4. Effect of Post-Processing on Microstructure of Ti-48Al-2Cr-2Nb Alloy

As mentioned earlier, although the Ti-48Al-2Cr-2Nb alloys formed using the EBSM process had high tensile properties, their plasticity was still very low. In addition, during the EBSM process, there were internal stresses inside the material. In order to resolve the above problems, this study employed heat treatment (HT: 900 °C/5 h), hot isostatic pressing (HIP: 1260 °C, 150 MPa/4 h), and a combination of hot isostatic pressing + heat treatment (HIP + HT) to reduce the internal stress in the material and improve the strength and elongation of the samples.

Figure 15 shows the metallographic structure of the Ti-48Al-2Cr-2Nb alloy prepared using the EBSM process after HIP treatment. As shown in the figure, the microstructure of the Ti-48Al-2Cr-2Nb alloy after HIP treatment in both the transverse and longitudinal directions was mainly composed of lamellar γ/α_2 phases and equiaxed γ phases, the grains of which were refined compared to those of the original microstructure (Figure 6). However, comparing Figure 16a–d, both the EBSM samples and HIP samples exhibited a coarse microstructure after the 900 °C/5 h heat treatment. Table 7 shows the relative density of the samples after different post-processing methods. In the table, we can see that the porosity of the samples after HIP and HIP + HT decreased significantly, and the relative density of the samples increased accordingly.

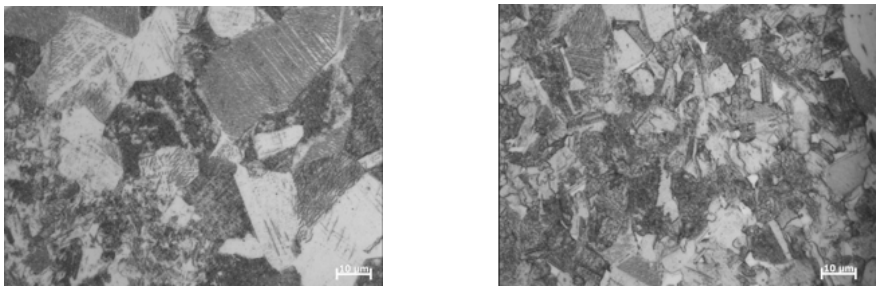

(**a**) (**b**)

Figure 15. Microstructure of Ti-48Al-2Cr-2Nb alloy before and after hot isostatic pressing treatment: (**a**) transverse; (**b**) longitudinal.

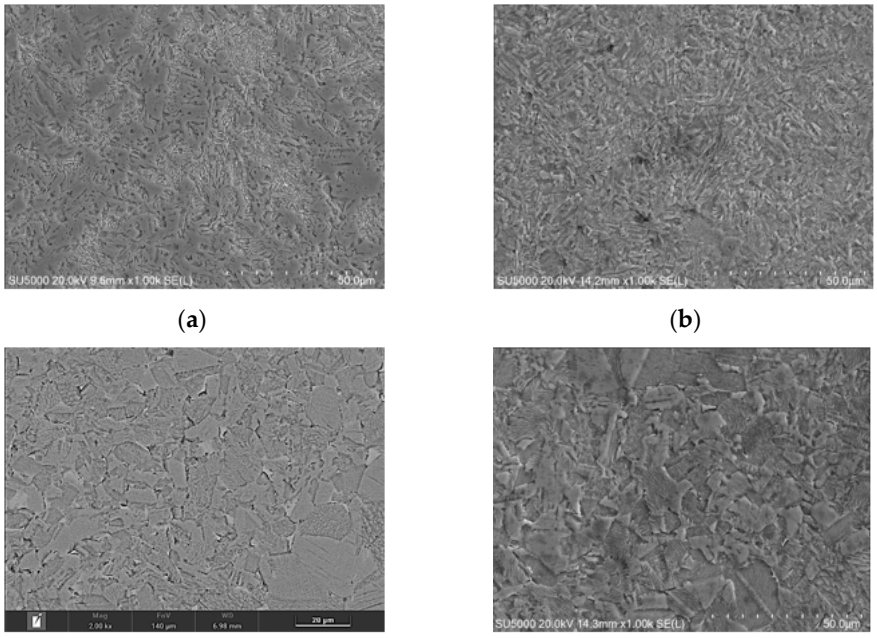

Figure 16. The effect of post-processing on the microstructure of Ti-48Al-2Cr-2Nb alloy: (**a**) EBSM; (**b**) HT; (**c**) HIP; (**d**) HIP + HT.

Table 7. Relative densities of samples after different post-processing methods.

Process	Relative Density (%)	Porosity (%)
EBSM	99.3	0.7
HT	99.4	0.6
HIP	99.8	0.2
HIP + HT	99.9	0.1

Figure 17 shows the distribution of elements inside the Ti-48Al-2Cr-2Nb alloy after different post-processing methods. As shown in the figure, with the progression of heat treatment, the samples after HT and HIP + HT exhibited an uneven distribution of Al, which indicates that there was a diffusion of the Al inside the material and the formation of new phases after post-processing. Further determination of the element contents showed that heat treatment did not alter the contents of various alloy elements inside the material (as shown in Table 8).

Table 8. Effect of post-processing on element contents of Ti-48Al-2Cr-2Nb alloy (wt.%).

Element	EBSM	HT	HIP	HIP + HT
Al	31.49	34.88	32.83	34.56
Ti	60.71	57.72	59.74	57.69
Cr	2.34	2.29	2.32	2.15
Nb	5.46	5.11	5.11	5.61
Total	100.00	100.00	100.00	100.00

EBSD analysis was performed on the Ti-48Al-2Cr-2Nb alloy before and after post-processing, and the results are shown in Figure 18. As shown in the figure, with the progress of post-processing, the content of the α_2 phases increased. Based on the XRD analysis of Ti-48Al-2Cr-2Nb alloy before and after post-processing (as shown in Figure 19), it can be seen that both the diffraction intensity of the γ phases and the α_2 phases increased.

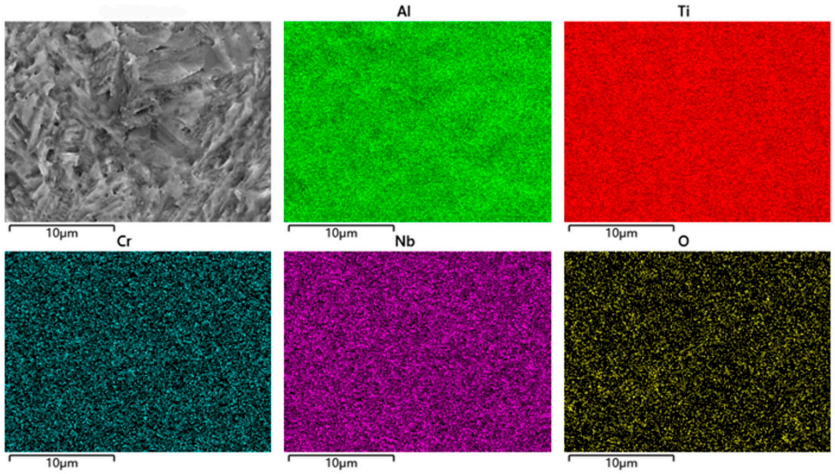

Figure 17. Distribution of elements inside Ti-48Al-2Cr-2Nb alloy after different post-processing methods: (**a**) HT; (**b**) HIP + HT.

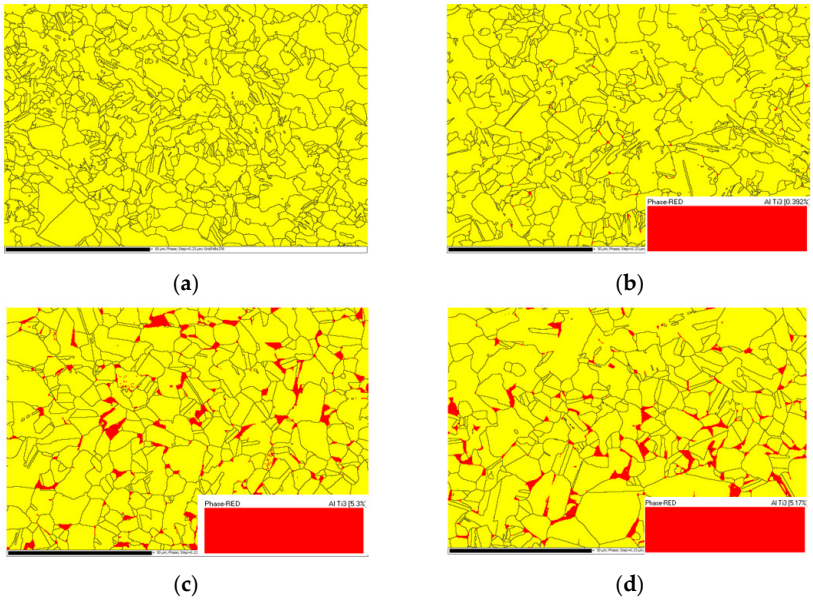

Figure 18. EBSD analysis of Ti-48Al-2Cr-2Nb alloy before and after post-processing (yellow is γ, red is α_2): (**a**) EBSM; (**b**) HT; (**c**) HIP; (**d**) HIP + HT.

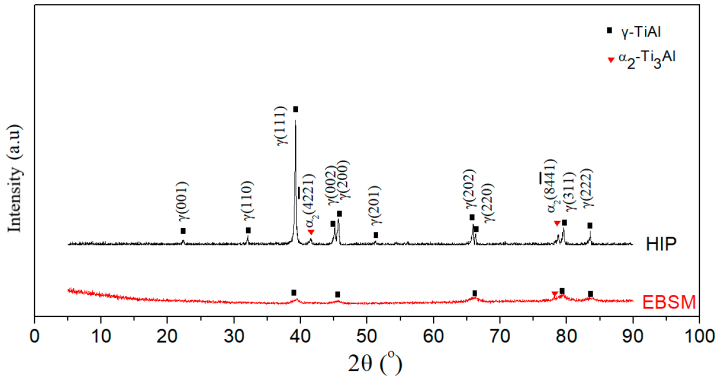

Figure 19. XRD analysis of phase structure in Ti-48Al-2Cr-2Nb alloy before and after HIP process.

TEM micrographs of the Ti-48Al-2Cr-2Nb alloy after the HT process are shown in Figure 20. As shown in the figure, the microstructure of the Ti-48Al-2Cr-2Nb alloy consisted of double phases composed of fine lamellar-structured α_2/γ and equiaxed γ phases (Figure 20a). The equiaxed γ phases were further analyzed, and dark field images are shown in Figure 20b. As can be seen in the figure, there were areas with lower brightness between the bright and wide lamellar γ phases. EDS analysis of this region revealed that the elemental composition was mainly Ti and Al, and the atomic ratio of the two was close to 2:1. Diffraction spots are also shown in Figure 20b, indicating that the lamellar phases between the equiaxed γ phases were B2 phases. In addition to the lamellar γ phases, massive γ phases and diffraction spots can also be observed in Figure 20c. Compared to the microstructure of the original Ti-48Al-2Cr-2Nb alloy formed using EBSM (Figure 7c), the dislocation density in the alloy after heat treatment was significantly reduced (Figure 20d).

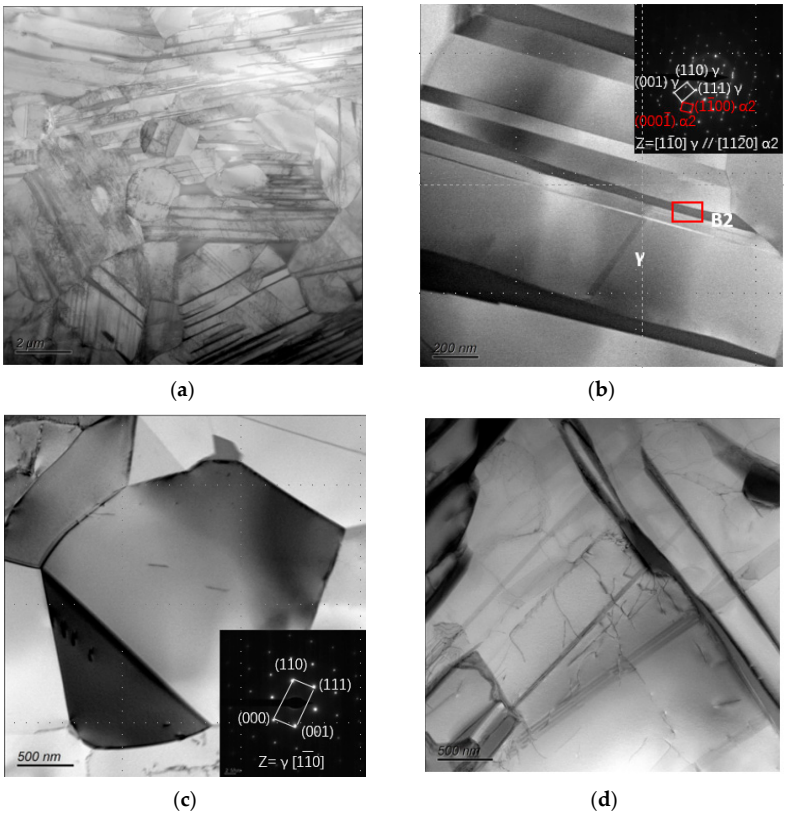

Figure 20. TEM micrographs of the Ti-48Al-2Cr-2Nb alloy after heat treatment process: (**a**) double-phase microstructure; (**b**) orientation relationship of B2 phases and γ phases; (**c**) γ phases and the diffraction spots; (**d**) dislocations.

A TEM micrograph of the Ti-48Al-2Cr-2Nb alloy after a hot isostatic pressing treatment is shown in Figure 21. Compared to the microstructure of the samples after EBSM, it can be seen that there was an increase in the content of phase γ and a decrease in phase B2 (Figure 21a,b), accompanied by the appearance of a massive structure of phase γ after HIP treatment. Figure 21c shows the morphology and diffraction patterns of phase γ. Moreover, due to the high-temperature and high-pressure treatment, the number of dislocations inside the material increased (Figure 21d).

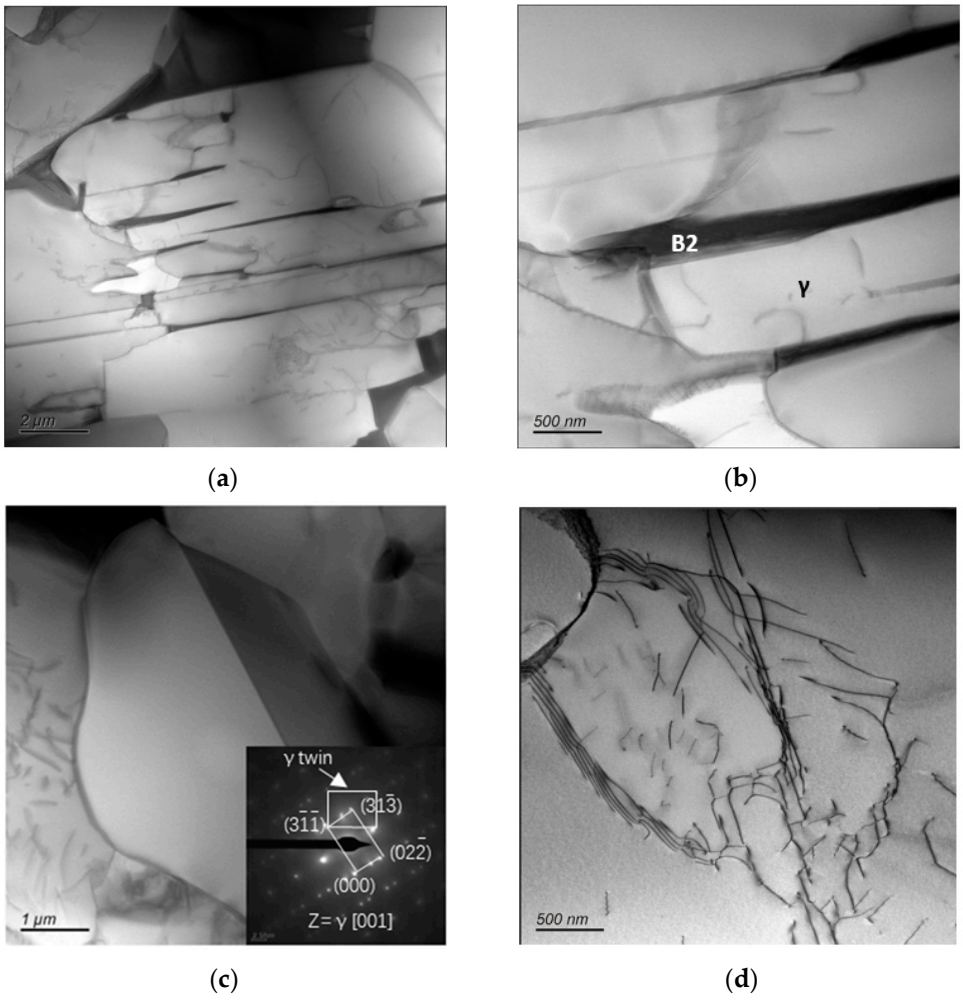

Figure 21. TEM micrographs of Ti-48Al-2Cr-2Nb alloy after hot isostatic pressing treatment process: (**a**) dual-phase microstructure; (**b**) B2 phase and γ phase; (**c**) γ phase twins and their diffraction spots; (**d**) dislocations.

Further heat treatment was performed on the Ti-48Al-2Cr-2Nb alloy after HIP at 900 °C, and the microstructure is shown in Figure 22. It can be seen in the figure that the phase composition of the microstructure consisted of phase γ and phase B2. At the same time, the dislocation density inside the material decreased compared to that in Figure 21a, and the B2 phase transformed from massive to lamellar. Figure 22b,c show the diffraction patterns of phase γ and phase B2, respectively.

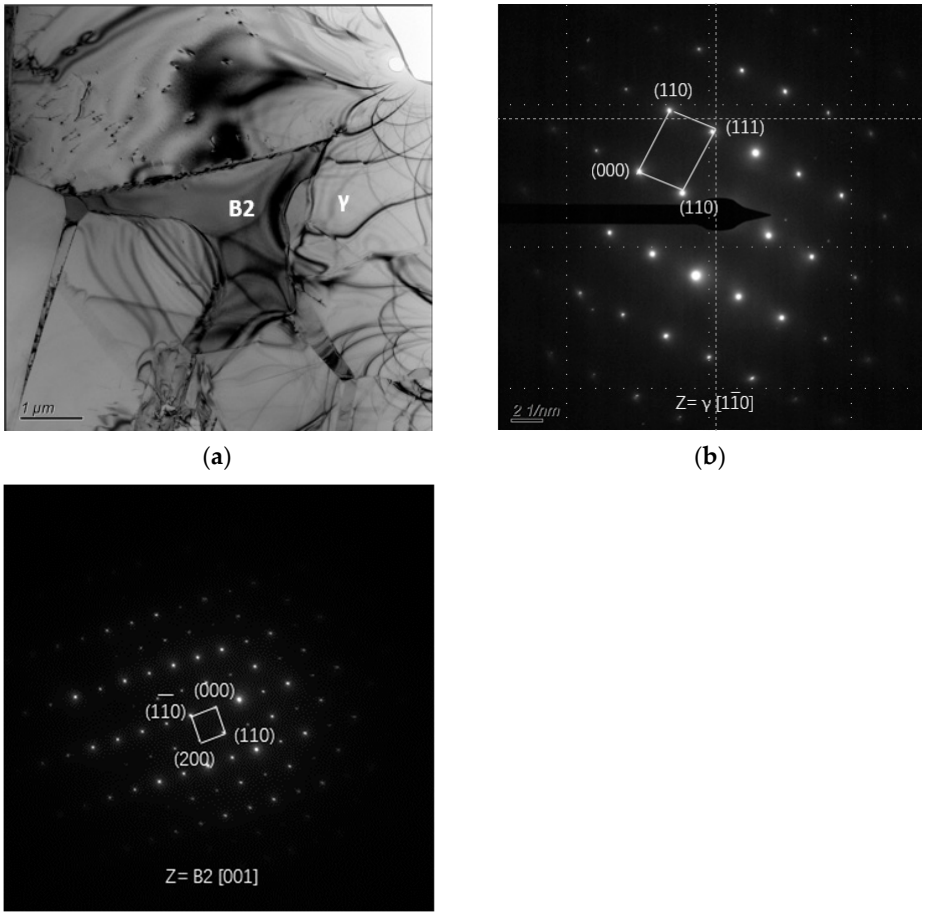

(**a**) (**b**)

(**c**)

Figure 22. TEM micrographs of Ti-48Al-2Cr-2Nb alloy after HIP + HT process: (**a**) dual-phase microstructure; (**b**) diffraction spots of γ phase; (**c**) diffraction spots of B2 phase.

3.5. Effect of Post-Processing on Mechanical Properties of Ti-48Al-2Cr-2Nb Alloy

Figure 23 shows the tensile curves of the Ti-48Al-2Cr-2Nb alloy before and after post-processing. As shown in the figure, the tensile curve of the Ti-48Al-2Cr-2Nb alloy after HIP treatment exhibits obvious plastic deformation characteristics. The Ti-48Al-2Cr-2Nb alloy fabricated in this study had a tensile strength of 679 MPa and an elongation of 2.5% after HIP treatment. The tensile strength and elongation of the HIP samples were much higher than those of the EBSM samples. This was mainly due to three factors [39]. Firstly, the relative density of the samples after HIP treatment was higher than that of the samples formed using EBSM. Secondly, as shown in Figure 18, the phase content of the material changed. The content of the α_2 phase was higher, resulting in higher resistance to deformation. At the same time, the relatively high amount of the γ phase in the HIP samples improved its ductility. Thirdly, the number of dislocations inside the material increased after HIP treatment. With the combined effects of the above factors, the strength and plasticity of the Ti-48Al-2Cr-2Nb alloy after HIP treatment were significantly improved. In the figure, it can clearly be seen that the mechanical properties of the samples (HIP + HT) were lower than that of the HIP samples. This was mainly related to the decrease in the dislocation density inside the material and the generation of a massive B2 phase.

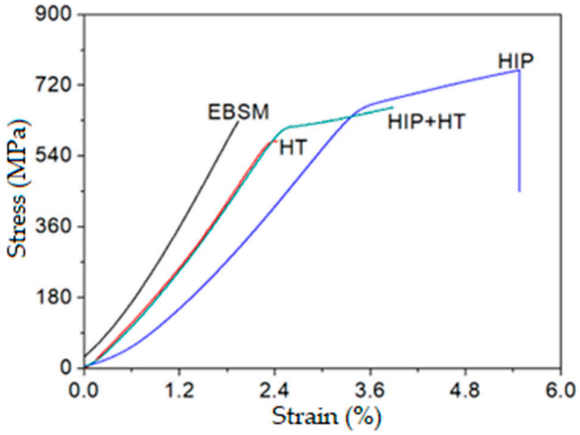

Figure 23. Tensile curves of Ti-48Al-2Cr-2Nb alloy before and after post-processing.

4. Conclusions

(1) The microstructures of the Ti-48Al-2Cr-2Nb alloys formed using the EBSM process were dense and composed of a γ phase, α_2 phase, and a small amount of B2 phase. Among them, the γ phase was equiaxed crystal, and there was no α_2 phase. The lamellar B2 phase was evenly distributed among the equiaxed γ phases. The α_2 phase was discontinuous and mainly distributed at the intersection of grain boundaries. In addition, a large number of dislocations formed due to thermal stress were also observed inside the Ti-48Al-2Cr-2Nb alloy. When the forming process parameters were 13.5 mA, 4.0 m/s, and 40.50 J/mm^3, as the current intensity increased, the Al element content decreased, the content of α_2 phase increased, and the microstructure of the material was coarse.

(2) The Ti-48Al-2Cr-2Nb alloy formed using the EBSM process exhibited brittle fracture during tensile deformation, lacking the typical yield deformation of metal materials. As the printing energy density increased, the mechanical properties of the Ti-48Al-2Cr-2Nb alloy first increased and then decreased. The samples prepared with an energy density of 34.50~40.50 J/mm^3 had excellent mechanical properties, with a tensile strength of over 620 MPa and a maximum value of 643 Mpa, an elongation rate of over 1.9%, and a maximum value of 2.09%.

(3) The microstructure of the Ti-48Al-2Cr-2Nb alloy after HIP treatment was mainly composed of a γ phase and α phase, the grains of which were refined compared to the microstructure of the EBSM samples. However, both the EBSM samples and HIP samples exhibited a coarse microstructure after the 900 °C/5 h heat treatment. There was an increase in the amount of γ phase and a decrease in B2 phase, accompanied by the generation of a massive γ phase after HIP treatment. Moreover, due to the high-temperature and high-pressure treatment, the number of dislocations inside the material increased. Further heat treatment was performed on the Ti-48Al-2Cr-2Nb alloy after HIP at 900 °C; the dislocation density inside the material decreased, and the B2 phase transformed from massive to lamellar.

(4) The Ti-48Al-2Cr-2Nb alloy after HIP treatment exhibited obvious plastic deformation characteristics, with a tensile strength of 679 MPa and elongation of 2.5%.

Author Contributions: Conceptualization, Y.Z.; methodology, M.S. and B.Z.; data curation, Y.L. (Yan Li), Y.L. (Yanchun Li) and S.G.; software, Y.L. (Yan Li), Y.L. (Yanchun Li) and S.G.; visualization, Y.L. (Yan Li), Y.L. (Yanchun Li) and S.G.; data analysis, B.Z.; resources, B.Z.; writing—original draft preparation, Y.Z.; writing—review and editing, M.S.; supervision; B.Z.; funding acquisition, Y.Z. All authors have read and agreed to the published version of the manuscript.

Funding: This research was funded by the Heilongjiang Provincial Institute Research Business Fee Project (Grant No. CZKYF2023-1-C039), and the Talent Team Construction Platform Project of Heilongjiang Academy of Sciences (RC2023GY01).

Institutional Review Board Statement: Not applicable.

Data Availability Statement: The data presented in this study are available on request from the corresponding author. The data are not publicly available due to privacy.

Conflicts of Interest: Yu Zhang, Yan Li, Meihui Song, Yanchun Li, Shulin Gong were employed by the company Institute of Advanced Technology. The remaining author declares that the research was conducted in the absence of any commercial or financial relationships that could be construed as a potential conflict of interest.

References

1. Kim, Y.W.; Kim, S.L. Advances in Gammalloy Materials–Processes–Application Technology: Successes, Dilemmas, and Future. *JOM* **2018**, *70*, 553–560. [CrossRef]
2. Hou, Z.; Li, B.; Feng, G.; Wu, J.; Fan, L.; Guo, Y.; Chen, Y.; Chen, B.; Zhang, X. Development and application of Ti-based alloy casting technologies in the field of aerospace. *Aerosp. Shanghai* **2022**, *39*, 14.
3. Wu, X. Review of alloy and process development of TiAl alloys. *Intermetallics* **2006**, *14*, 1114–1122. [CrossRef]
4. Cho, K.; Morita, N.; Matsuoka, H. Influence of Input Energy Density on Morphology of Unique Layered Microstructure of γ-TiAl Alloys Fabricated by Electron Beam Powder Bed Fusion. *Mater. Trans.* **2023**, *64*, 44–49. [CrossRef]
5. Bewlay, B.P.; Nag, S.; Suzuki, A.; Weimer, M.J. TiAl alloys in commercial aircraft engines. *Mater. High Temp.* **2016**, *33*, 549–559. [CrossRef]
6. Gao, R.; Peng, H.; Guo, H.; Chen, B. An innovative way to fabricate γ-TiAl blades and their failure mechanisms under thermal shock. *Scr. Mater.* **2021**, *203*, 114092. [CrossRef]
7. Chen, W.; Li, Z. Additive manufacturing of titanium aluminides. In *Additive Manufacturing for the Aerospace Industry*; Elsevier: Amsterdam, The Netherlands, 2019; pp. 235–263.
8. Liu, N.; Niu, J.; Chen, Y.; Wang, X.; Wang, J.; Xiang, H.; Wei, D.; Chen, G. Effect of in-situ post-heating on the microstructure and tensile performance of TiAl alloys produced via selective electron beam melting. *Mater. Sci. Eng. A* **2023**, *885*, 145585. [CrossRef]
9. Ghibaudo, C.; Marchese, G.; Ugues, D.; Biamino, S.; Wartbichler, R.; Clemens, H. Influence of focus offset on the microstructure of an intermetallic γ-TiAl based alloy produced by electron beam powder bed fusion. *J. Manuf. Process* **2023**, *89*, 132–141. [CrossRef]
10. Kotzem, D.; Teschke, M.; Juechter, V.; Krner, C.; Walther, F. Microstructure analysis and mechanical properties of electron beam powder bed fusion (PBF-EB)-manufactured γ-titanium aluminide (TiAl) at elevated temperatures. *Mater. Test.* **2022**, *64*, 636–646. [CrossRef]
11. Lin, B.; Chen, W. Mechanical properties of TiAl fabricated by electron beam melting—A review. *China Foundry* **2021**, *18*, 307–316. [CrossRef]
12. Knorlein, J.; Franke, M.M.; Schloffer, M.; Korner, C. In-situ aluminum control for titanium aluminide via electron beam powder bed fusion to realize a dual microstructure. *Addit. Manuf.* **2022**, *59*, 103132.
13. Liu, J.; Zhang, L. A Study of Compression Deformation Behavior of γ/α2 Interface in γ (TiAl) Alloy Using Molecular Dynamics Simulation. *J. Mater. Eng. Perform.* **2024**, *33*, 483–495. [CrossRef]
14. Schwerdtfeger, J.; Korner, C. Selective electron beam melting of Ti–48Al–2Nb–2Cr: Microstructure and aluminium loss. *Intermetallics* **2014**, *49*, 29–35. [CrossRef]
15. Kan, W.; Chen, B.; Jin, C.; Peng, H.; Lin, J. Microstructure and mechanical properties of a high Nb-TiAl alloy fabricated by electron beam melting. *Mater. Des.* **2018**, *16*, 611–623. [CrossRef]
16. Xu, R.; Li, M.; Zhao, Y. A review of microstructure control and mechanical performance optimization of γ-TiAl alloys. *J. Alloy Compd.* **2023**, *932*, 167611. [CrossRef]
17. Bieske, J.; Franke, M.; Schloffer, M.; Korner, C. Microstructure and properties of TiAl processed via an electron beam powder bed fusion capsule technology. *Intermetallics* **2020**, *126*, 106929. [CrossRef]
18. Umakoshi, Y.; Nakano, T. The role of ordered domains and slip mode of α2 phase in the plastic behaviour of TiAl crystals containing oriented lamellae. *Acta Metall. Mater* **1993**, *41*, 1155–1161. [CrossRef]
19. Wartbichler, R.; Clemens, H.; Mayer, S.; Ghibaudo, C.; Rizza, G.; Galati, M.; Iuliano, L.; Biamino, S.; Ugues, D. On the formation mechanism of banded microstructures in electron beam melted Ti–48Al–2Cr–2Nb and the design of heat treatments as remedial action. *Adv. Eng. Mater.* **2021**, *23*, 12. [CrossRef]
20. Chen, X.; Tang, B.; Liu, D.; Wei, B.; Zhu, L.; Liu, R.; Kou, H.; Li, J. Dynamic recrystallization and hot processing map of Ti-48Al-2Cr-2Nb alloy during the hot deformation. *Mater. Charact.* **2021**, *179*, 111332. [CrossRef]
21. Galati, M.; Rizza, G.; Salmi, A.; Biamino, S.; Ghibaudo, C.; Fino, P.; Iuliano, L. Residual stress investigation on Ti-48Al-2Cr-2Nb samples produced by Electron Beam Melting process. *Procedia CIRP* **2021**, *99*, 336–341. [CrossRef]
22. Reith, M.; Franke, M.; Schloffer, M.; Korner, C. Processing 4th generation titanium aluminides via electron beam based additive manufacturing—Characterization of microstructure and mechanical properties. *Materialia* **2020**, *14*, 100902. [CrossRef]
23. Peters, S.; Perez, M.; Blackwell, P. Integrating HIP and homogenisation heat treatment and its effect on the workability of a conventional peritectic TiAl alloy. *Intermetallics* **2023**, *158*, 107884. [CrossRef]
24. Yue, H.; Chen, Y.; Wang, X.; Kong, F. Effect of beam current on microstructure, phase, grain characteristic and mechanical properties of Ti-47Al-2Cr-2Nb alloyfabricated by selective electron beam melting. *J. Alloys Compd.* **2018**, *750*, 449–458. [CrossRef]

25. Tang, H.P.; Yang, G.Y.; Jia, W.P.; He, W.W.; Lu, S.L.; Qian, M. Additive manufacturing of a high niobium-containing titanium aluminide alloy by selective electron beam melting. *Mater. Sci. Eng. A* **2015**, *636*, 103–107. [CrossRef]
26. Cho, K.; Kawabata, H.; Hayashi, T.; Yasuda, H.Y.; Nakano, T. Peculiar microstructural evolution and tensile properties of β-containing γ-tial alloys fabricated by electron beam melting. *Addit. Manuf.* **2021**, *46*, 102091. [CrossRef]
27. Ikeo, N.; Ishimoto, T.; Nakano, T. Novel powder/solid composites possessing low Young's modulus and tunable energy absorption capacity, fabricated by electron beam melting, for biomedical applications. *J. Alloys Compd.* **2015**, *639*, 336–340. [CrossRef]
28. Yue, H.; Peng, H.; Li, R.; Qi, K.; Zhang, L.; Lin, J.; Su, Y. Effect of heat treatment on the microstructure and anisotropy of tensile properties of TiAl alloy produced via selective electron beam melting. *Mater. Sci. Eng. A* **2021**, *803*, 140473. [CrossRef]
29. Chen, Y.; Yue, H.; Wang, X.; Xiao, S.; Kong, F.; Cheng, X.; Peng, H. Selective electron beam melting of TiAl alloy: Microstructure evolution, phase transformation and microhardness. *Mater. Charact.* **2018**, *142*, 584–592. [CrossRef]
30. Flemings, M.C. Solidification processing. *Met. Mater. Trans.* **1974**, *B5*, 2121–2134. [CrossRef]
31. Sakata, M.; Oh, J.Y.; Cho, K.; Yasuda, H.Y.; Todai, M.; Nakano, T.; Ikeda, A.; Ueda, M.; Takeyama, M. Effects of heat treatment on unique layered microstructure and tensile properties of TiAl fabricated by electron beam melting. *Mater. Sci. Forum* **2018**, *941*, 1366–1371. [CrossRef]
32. Chen, Y.; Yue, H.; Wang, X. Microstructure, texture and tensile property as a function of scanning speed of Ti-47Al-2Cr-2Nb alloy fabricated by selective electron beam melting. *Mater. Sci. Eng. A* **2018**, *713*, 195–205. [CrossRef]
33. Appel, F.; Clemens, H.; Fischer, F.D. Modeling concepts for intermetallic titanium aluminides. *Prog. Mater. Sci.* **2016**, *81*, 55–124. [CrossRef]
34. Yue, H.; Peng, H.; Miao, K.; Gao, B.; Wu, H.; Yang, J. Significant enhancement in high-temperature tensile strength of trace nano-Y_2O_3-reinforced TiAl alloy prepared by selective electron beam melting. *Mater. Sci. Eng. A* **2023**, *875*, 5. [CrossRef]
35. Yue, H.; Liang, Z.; Zhang, F.; Fang, L.; Chen, P.; Xu, L.; Xiao, S.; Li, R. Effect of heat treatment on the microstructure and creep properties of ti-48al-2cr-2nb alloy produced by selective electron beam melting. *Mater. Sci. Eng. A* **2022**, *859*, 144224. [CrossRef]
36. *GB/T 3620.1-2016*; Code for Designation and Composition of Titanium and Titanium Alloys. China Nonferrous Metals Standardization Technical Committee: Beijing, China, 2016.
37. Gokan, K.; Yamagishi, Y.; Mizuta, K. Effect of process parameters on the microstructure and high-temperature strengths of titanium aluminide alloy fabricated by electron beam melting. *Mater. Trans.* **2023**, *64*, 104–110. [CrossRef]
38. Yan, Y.Q.; Zhang, Z.Q.; Luo, G.Z.; Wang, K.G.; Zhou, L. Microstructures observation and hot compressing tests of TiAl based alloy containing high Nb. *Mater. Sci. Eng. A* **2000**, *280*, 187–191. [CrossRef]
39. Liu, J.; Staron, P.; Riekehr, S.; Stark, A.; Schell, N.; Huber, N.; Schreyer, A.; Müller, M.; Kashaev, N. In situ study of phase transformations during laser-beam welding of a TiAl alloy for grain refinement and mechanical property optimization. *Intermetallics* **2015**, *62*, 35–48. [CrossRef]